ACS Catalysis

Research Article

pubs.acs.org/acscatalysis

Nanoshaped CuO/CeO_2 Materials: Effect of the Exposed Ceria Surfaces on Catalytic Activity in N_2O Decomposition Reaction

Maxim Zabilskiy,[†] Petar Djinović,[†] Elena Tchernychova,[‡] Olga P. Tkachenko,[§] Leonid M. Kustov,[§] and Albin Pintar*[,†]

[†]Laboratory for Environmental Sciences and Engineering and [‡]Laboratory for Materials Chemistry, National Institute of Chemistry, Hajdrihova 19, SI-1001 Ljubljana, Slovenia

[§]N.D. Zelinsky Institute of Organic Chemistry, Russian Academy of Sciences, Leninsky Prospect 47, Moscow 119991, Russia

Supporting Information

ABSTRACT: This study reports a thorough investigation of nanosized CuO/CeO_2 materials as an efficient catalyst for decomposition of N_2O, which is a strong greenhouse gas largely produced by chemical industry. Effect of terminating CeO_2 crystalline planes ({100}, {110}, and {111}) on the behavior of CuO dispersed over CeO_2 nanocubes, nanorods and polyhedral crystallites was examined in detail by using a variety of catalyst characterization techniques. The 4 wt % Cu was found as the most advantageous metal loading, whereas higher Cu content resulted in lower dispersion and formation of significantly less active, segregated bulk CuO phase. It was discovered that CuO/CeO_2 solids should enable both excessive oxygen mobility on the catalyst surface as well as formation of highly reducible Cu defect sites, in order to ensure high intrinsic activity. Detailed studies further revealed that CeO_2 morphology needs to be tailored to expose {100} and {110} high-energy surface planes, as present in CeO_2 nanorods. Oxygen mobility and regeneration of active Cu phase on these surface planes is easier, which in turn facilitates higher catalytic activity through the recombination of surface oxygen atoms and desorption as molecular oxygen that replenishes active sites for subsequent catalytic cycles. As a consequence, CuO supported on CeO_2 nanorods demonstrated lower activation energy (87 kJ/mol) in N_2O decomposition reaction compared to catalysts based on CeO_2 nanocubes (102 kJ/mol) or polyhedral CeO_2 (92 kJ/mol).

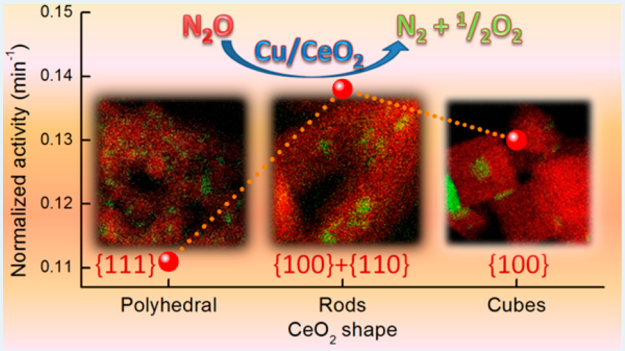

KEYWORDS: *N_2O decomposition, CuO defect sites, structure−activity relationship, redox catalyst, nanoshaped CeO_2*

1. INTRODUCTION

Cerium dioxide (CeO_2) is a versatile material in heterogeneous catalysis, solid oxide fuel cells, solar cells, and oxygen membranes.[1−3] It is often used to support transition or noble metals and provide distinctive catalytic functionality, for example in PROX, WGS, and H_2O_2 synthesis reactions.[4−7] Tailored CeO_2 nanomorphology such as cubes or rods can result in drastic improvement of CeO_2-mediated catalytic performance in reactions where redox property of a catalyst is crucial, compared to randomly shaped CeO_2 crystallites.[8−11] This manifests itself through different selectivity or improved activity, which enables the catalyst to be operated at lower temperatures. Numerous theoretical[12−14] and experimental[8−11,15−21] investigations have revealed that nanoshaped CeO_2 (nanocubes and nanorods) with well-defined {100} and {110} reactive planes show higher catalytic activity than conventional and thermodynamically more stable polyhedral CeO_2 nanoparticles. This is likely connected to lower activation energy for oxygen vacancy formation over {110} and {100} planes, compared to {111}.[22] The benefit of nanoshaping CeO_2 is dependent on particular reaction, where this catalyst is utilized. For example, catalysts based on CeO_2 nanorods were more active and selective in NO reduction,[8] catalytic oxidation of ethanol in air,[16] oxidative dehydrogenation of methanol,[9] catalytic combustion of chlorobenzene,[17] and water−gas shift (WGS) reaction,[10] while catalysts based on CeO_2 nanocubes showed superior properties in soot combustion,[11] hydrogen oxidation,[18] and CO-PROX.[19]

In this work, catalytic N_2O decomposition over CuO supported on nanoshaped CeO_2 was investigated. Catalysts commercially used for N_2O abatement (CuO/Al_2O_3, $La_{0.8}Ce_{0.2}CoO_3$, Co_2AlO_4/CeO_2, and Fe-ZSM-5) require either high operating temperatures or addition of reducing agents.[23,24] Among the catalysts which can decompose N_2O under moderate temperatures (300−500 °C), CuO/CeO_2 materials show very promising results.[25−28] Interest in N_2O decomposition arises from the fact that it is a potent greenhouse gas, produced in nitric acid and fertilizer industry, which contributes

Received: May 19, 2015
Revised: July 14, 2015
Published: July 31, 2015

DOI: 10.1021/acscatal.5b01044
ACS Catal. 2015, 5, 5357−5365

to ozone layer depletion.[29,30] As a result, understanding and design of the catalyst that enables its efficient destruction is of great importance. In N_2O decomposition reaction, coupling of adjacent surface oxygen atoms and desorption (as molecular oxygen) governs the overall reaction rate.[31] Fast replenishment of the catalytically active sites through weakening the M−O bond provides the leverage for boosting the catalytic activity. This is expected to be achieved by increasing oxygen mobility in CuO/CeO_2 catalysts.

Adamski et al. have studied N_2O decomposition using 5 mol % CuO/CeO_2 catalysts.[25] They have supported their experimental results by quantum chemical DFT modeling, where the most stable {111} surface of CeO_2 was modified with copper by replacing Ce^{4+} cations with Cu^{2+} and the creation of an adjacent oxygen vacancy. Calculations have confirmed the dominating role of oxygen atom recombination and desorption steps on catalyst activity. Zhou et al., who investigated an influence of copper loading in the CuO/CeO_2 catalyst on N_2O decomposition activity, discovered that at low copper loadings stronger synergetic effect between CuO and CeO_2 takes place, which results in good catalytic performance of studied solids.[26] Our previous work was dedicated to the enhancement of catalytic activity by using high surface area (HSA) CeO_2 support (S_{BET} = 190 m^2/g), prepared by means of glycothermal method.[27,28] The highest activity of CuO/CeO_2 catalyst was obtained in the presence of subnanometer CuO clusters on HSA CeO_2. It should be noted that all previous studies were carried out over random, polyhedral CeO_2 nanoparticles; therefore, the role of CeO_2 morphology and exposed crystalline planes to act as a leverage to boost N_2O decomposition activity remains unknown. This was investigated in the present study. The correlation between catalytic properties of examined materials as well as their chemical state and morphology was made possible by using HRTEM, STEM-HAADF, STEM-EDX, N_2 physisorption, DR-UV−vis, in situ DRIFTS CO, XRD, XPS, H_2-TPR, and dissociative N_2O adsorption techniques.

2. EXPERIMENTAL SECTION

2.1. Catalyst Synthesis. CeO_2 nanocubes (CeO_2-C) and nanorods (CeO_2-R) were synthesized by dissolving 53.8 g of NaOH (99% purity, Merck) in 140 mL of deionized water. Then, 84 mL of aqueous solution containing 4.9 g of $Ce(NO_3)_3{\cdot}6H_2O$ (99% purity, Sigma-Aldrich) was added under vigorous stirring. The suspension was stirred for additional 30 min and transferred into a Teflon-lined stainless steel autoclave. For preparation of CeO_2-C and CeO_2-R samples, suspension was aged 24 h at 180 and 100 °C, respectively. Aged suspensions were centrifuged at 5000 rpm and washed with deionized water until reaching pH = 7. The obtained solids were dispersed in 10 mL of deionized water, frozen by quench-freezing with LN_2 and finally dried for 24 h using freeze-dryer (Christ, model Alpha 1-2 LDplus). The samples were calcined in air at 400 °C for 3 h (heating ramp 2 °C/min). For preparation of polyhedral CeO_2 nanoparticles (CeO_2-P), synthesis conditions were identical to those of CeO_2-R with one exception: 8.96 g of NaOH was utilized instead of 53.8 g.

The following method was applied for depositing 2−8 wt % Cu over CeO_2 supports: 400 mg of CeO_2 (cubes, rods, or polyhedral nanoparticles) was dispersed in 10 mL of deionized water using an ultrasonic homogenizer (Cole-Parmer) and an appropriate amount of $Cu(NO_3)_2{\cdot}3H_2O$ (99.5% purity, Sigma-Aldrich) was added to reach the nominal loading. Then, 5 mL of aqueous solution containing 250 mg of Na_2CO_3 (99.999% purity, Merck) was added under vigorous stirring. The formed suspension was stirred at room temperature for additional 2 h, filtered, washed with 150 mL of deionized water, redispersed in 5 mL of deionized water and dried in a freeze drier for 24 h. The obtained solid was calcined in air at 400 °C for 3 h (heating ramp 2 °C/min). Prepared materials were marked as *X*-Cu/CeO_2-*M*, where *X* represents Cu content in weight percent accordingly to synthesis conditions and *M* represents morphology of utilized CeO_2 supports—cubes, rods, or polyhedra.

2.2. Catalyst Characterization. BET specific surface area, total pore volume and pore size distribution was determined at −196 °C using a TriStar II 3020 instrument from Micromeritics. Prior to measurements, samples were degassed in N_2 stream (purity 6.0, Linde) at 90 °C for 1 h, followed by 3 h soaking at 300 °C using the Micromeritics SmartPrep degasser. The Brunauer−Emmett−Teller (BET) method was applied for specific surface area calculations. The pore size distributions were derived from the desorption branch of the isotherms employing the Barrett−Joyner−Halenda (BJH) method. The total pore volume was estimated at a relative pressure of 0.989.

X-ray diffraction measurements were performed on a PANalytical X'pert PRO diffractometer equipped with the monochromator for Cu Kα1 radiation, λ = 0.15406 nm. Materials were scanned in the 2θ range between 10° and 85° with 0.0348° increments, respectively, and 100 s measuring time at each increment.

H_2 temperature-programmed reduction (H_2-TPR) experiments were performed using a Micromeritics AutoChem II 2920 apparatus. Examined samples (approximately 100 mg) were preoxidized at 300 °C in 5 vol % O_2/N_2 and cooled to −40 °C. TPR analysis was performed in a 25 mL/min stream of 5 vol % H_2/Ar mixture. The samples were heated from −40 to 900 °C (CeO_2 supports) or to 500 °C (CuO/CeO_2 materials) with a 5 °C/min ramp during analysis. Deconvolution of recorded TPR profiles was performed in Origin 8.1 software using Gaussian and Lorentzian functions. Immediately following H_2-TPR examination, dissociative N_2O adsorption experiment was done for selected samples in order to determine Cu dispersion and cluster size. To selectively probe only metallic copper surface sites and avoid titration of oxygen defect sites of CeO_2 support,[32] N_2O pulsing (10 vol % N_2O/He) was performed at 35 °C. Decomposition of N_2O and formation of N_2 were monitored with a TCD detector (a LN_2 cold trap was mounted on exhaust in order to condense unreacted N_2O, so only N_2 formed during N_2O pulse titration was detected by the TCD detector).

UV−vis diffuse reflectance spectra of synthesized materials were recorded at room temperature (RT) using a PerkinElmer Lambda 35 UV−vis spectrophotometer equipped with the RSA-PE-19 M Praying Mantis accessory. Pure CeO_2-C, CeO_2-R, and CeO_2-P supports were utilized to perform the instrument background correction in the range of 200−1100 nm. The scans were acquired with the speed of 120 nm/min, and the slit was set to 4 nm.

The diffuse reflectance Fourier transform infrared (DRIFT) spectra were recorded in the range of 400−4000 cm^{-1} using a FT-IR analyzer (PerkinElmer, model Frontier), equipped with a DRIFT cell and high temperature reaction chamber (Pike Technologies, model DiffusIR). Prior to CO adsorption, the samples were degassed in situ at 300 °C and N_2 flow for 30 min. After degassing, the samples were cooled to 35 °C and

DOI: 10.1021/acscatal.5b01044
ACS Catal. 2015, 5, 5357−5365

exposed to 10 vol % CO/N_2 mixture for 10 min, followed by N_2 purging (50 mL/min) for 30 min. Spectra were collected at 35 °C with the resolution of 4 cm^{-1} and accumulation of 16 scans. During temperature-programmed desorption of CO, temperature was increased from 35 to 450 °C (heating rate 10 °C/min in N_2 flow) and every 15 s the FTIR spectrum was recorded. Analysis of recorded FTIR spectra was performed in Origin 8.1 software.

X-ray photoelectron spectra were measured with ES-2403 modified spectrometer (Russia) equipped with a PHOIBOS 100 MCD analyzer (Specs GmbH), using Mg Kα excitation (1253.6 eV, 10 kV, and 25 mA). The spectrometer was calibrated by binding energy (BE) of Au $4f_{7/2}$ = 84.0 eV and Ni $2p_{3/2}$ = 852.7 eV. Detailed spectra were recorded for the regions of Cu 2p, Ce 3d photoelectrons and Cu L_3VV Auger electrons with a 0.1 eV step at a pressure below 3×10^{-6} Pa. Data acquisition was realized by the SpecsLab2 software and analysis was performed by the CasaXPS software. The binding energy of XPS peaks (with the accuracy of ±0.1 eV) was corrected by referencing to the Ce $3d_{5/2}$ peak at 882.0 eV (internal standards).

Morphology of synthesized materials was studied by means of high-resolution transmission electron microscopy (HRTEM) and scanning TEM high-angle annular dark field imaging (STEM-HAADF). Copper distribution was assessed by energy-dispersive X-ray spectroscopy in STEM mode (STEM-EDX). For these analyses, a probe aberration-corrected JEM-ARM200CF equipped with JEOL Centurio 100 mm^2 EDXS detector and JEOL STEM detectors (JEOL, Tokyo, Japan) was employed.

2.3. Catalytic Experiments. Catalytic N_2O decomposition activity was tested in a fixed-bed quartz reactor using 50 mg of catalyst, diluted with 200 mg of SiC. Powdered catalyst was positioned inside the 9 mm I.D. quartz tube and fixed between two quartz wool beads. Prior to tests, catalysts were in situ activated in Ar flow (50 mL/min) at 400 °C for 2 h (heating rate 2 °C/min). N_2O decomposition was performed at atmospheric pressure in the temperature range between 300 and 550 °C. N_2O feed concentration was 2500 ppm, balanced by Ar, while the gas flow rate was equal to 100 mL/min (WHSV = 120 L/(g_{cat} h)). At each reaction temperature, the catalyst was allowed to stabilize for 30 min before analyzing the gas stream discharged from the reactor. Analysis of reaction products and remaining N_2O at the reactor outlet was performed by gas chromatography using Agilent 490 Micro GC (Agilent Technologies) equipped with 10 m MS5A and 10 m Porabond Q columns.

3. RESULTS AND DISCUSSION

3.1. Material Characterization. N_2 physisorption revealed a considerable difference in BET specific surface of synthesized nanoshaped CeO_2 supports (Table 1). The following decreasing trend can be established: CeO_2-P > CeO_2-R > CeO_2-C. The obtained values are in good agreement with the results of other works.[9]

Reducibility of prepared CeO_2 supports (measured by using H_2-TPR technique) is provided in Table 1 and Figure 1. H_2-TPR profile of CeO_2 usually comprises two reduction peaks, which are attributed to a two-step reduction mechanism: low-temperature reduction of surface-capping Ce^{4+}, followed by reduction of bulk CeO_2 at higher temperature.[11,33−35] The CeO_2-P and CeO_2-R samples exhibit a low-temperature peak between 200 and 560 °C and a high temperature peak between

Table 1. Physical−Chemical Properties of Synthesized Nanoshaped CeO_2 Supports

sample	S_{BET} (m^2/g)	crystallite size[a] (nm)	H_2 consumption[b] (cm^3/g)	reduction of Ce^{4+} to Ce^{3+} [c] (%)
CeO_2-C	29	27	3.6	19.8
CeO_2-R	87	11	10.4	29.4
CeO_2-P	115	8	15.5	39.2

[a]Calculated using Scherrer equation accordingly to the (111) diffraction peak of CeO_2. [b]Evaluated from H_2 consumed between −40 and 560 °C. [c]Evaluated from H_2 consumed between −40 and 900 °C.

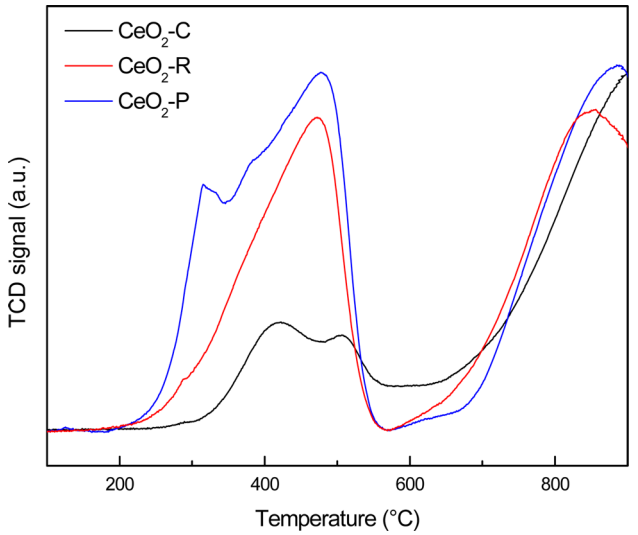

Figure 1. H_2-TPR profiles of nanoshaped CeO_2 supports.

700 and 900 °C. In the case of CeO_2-C sample, low-temperature peak is much weaker and reduction occurs predominantly at temperatures above 600 °C. This difference is related to considerably lower BET specific surface area of CeO_2-C solid compared to CeO_2-P and CeO_2-R samples, and as a result to lower fraction of reducible surface Ce^{4+} ions.[36] If we consider the average CeO_2 crystallite size, calculated from XRD analysis as representative, then the H_2 amount consumed between 200 and 560 °C suffices for 0.9, 1.8, and 1.0 monolayers of CeO_2 reduction in CeO_2-C, CeO_2-R, and CeO_2-P samples, respectively, indicating that the assigned TPR signal indeed originates from surface CeO_2 reduction.

TEM micrographs presented in Figure 2 show that the nanoshaped CeO_2 supports maintain their authentic morphology after the Cu deposition. The CeO_2-C material (Figure 2a) consists of nanoparticles exhibiting a cubic morphology with the dimensions between 13 and 55 nm with the average particle size being ~21 nm. The determined interplanar spacing of 0.27 nm (HRTEM image on the inset) corresponds to the {200} type lattice planes, which leaves {100} type planes exposed as a surface terminating plane. It should be noted that truncated nanocubes with the {110} type planes and particles with polyhedral morphology were also observed in the CeO_2-C sample, however, only in a small fraction of less than 5%.

Size of the investigated ceria nanorods (CeO_2-R, Figure 2b) is between 80 and 140 nm in length and with the average width being ~8 nm. Interplanar spacings determined from the STEM-HAADF image on the inset are 0.27 and 0.19 nm, respectively,

DOI: 10.1021/acscatal.5b01044
ACS Catal. 2015, 5, 5357−5365

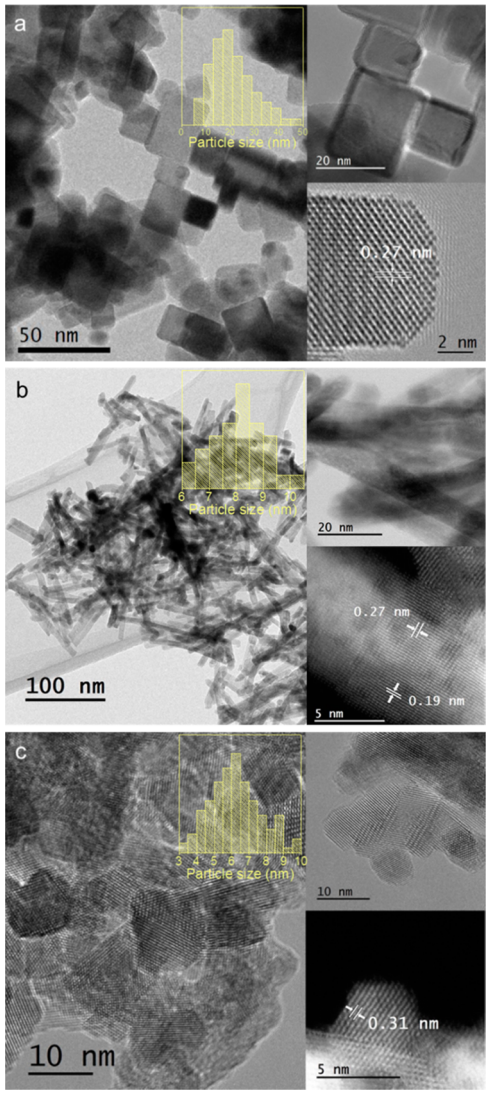

Figure 2. TEM images of 4-Cu/CeO_2-C (a), 4-Cu/CeO_2-R (b), and 4-Cu/CeO_2-P (c) catalysts.

which corresponds to {200} and {220} type lattice planes of CeO_2.

Figure 2c shows CeO_2-P sample, which is composed of nanoparticles of irregular morphologies with the average particle size being 6.5 nm. The {111} lattice fringes with interplanar spacing of 0.31 nm were identified from the STEM-HAADF micrograph shown on the inset. Based on TEM analysis, it can be concluded that synthesized nanoshaped CuO/CeO_2 materials terminate with different planes.

Diffraction patterns of materials containing 6 wt % Cu are illustrated in Figure S1. The main reflections could be assigned to FCC CeO_2 (PDF data file 03-065-5923). Only in 6-Cu/CeO_2-C sample, very small peaks belonging to most intensive $(1\bar{1}1)$ and (111) reflections of CuO (PDF 00-048-1548) were observed as a result of its lowest BET specific surface area, which consequently results in lower CuO dispersion. For solids containing 2 and 4 wt % of Cu, no diffraction peaks belonging to ordered copper phase can be detected.

In order to determine the particle size of CuO, STEM-HAADF, STEM-EDX, and N_2O titration techniques were utilized (Table 2). Two series of materials were analyzed: catalysts containing the same copper loading on differently

Table 2. Results of N_2O Adsorption Measurements

sample	Cu dispersion (%)	d_{Cu}[a] (nm)
2-Cu/CeO_2-R	60.2	1.8
4-Cu/CeO_2-C	21.7	5.1
4-Cu/CeO_2-R	45.7	2.4
4-Cu/CeO_2-P	52.4	2.1
6-Cu/CeO_2-R	35	3.1
8-Cu/CeO_2-R	20.3	5.4

[a]Measured by means of dissociative N_2O adsorption.

shaped supports (i.e., 4-Cu/CeO_2-C, 4-Cu/CeO_2-R, and 4-Cu/CeO_2-P samples) and materials based on the same support but having different Cu contents (i.e., 2-Cu/CeO_2-R, 4-Cu/CeO_2-R, 6-Cu/CeO_2-R, and 8-Cu/CeO_2-R samples). In the first group of solids, the Cu dispersion increased with increasing BET specific surface area (21.7, 45.7, and 52.4% for 4-Cu/CeO_2-C, 4-Cu/CeO_2-R, and 4-Cu/CeO_2-P catalysts, respectively). With increasing Cu loading from 2 to 8 wt %, Cu dispersion decreased from 60.2 to 20.3% on CeO_2-R support, which corresponds to an increase of CuO cluster size from 1.8 to 5.4 nm.

The STEM-EDX analysis was performed for samples containing 4 wt % of Cu (Figure 3). The 4-Cu/CeO_2-C sample showed nonuniform size distribution of the Cu-containing particles, with the particles sizes ranging from 3 to 15 nm (Figure 3a). More homogeneous Cu distribution was observed on CeO_2-R and CeO_2-P samples. Cu-containing particles size for these two samples varied from 1.5 to 4.5 nm, with the average size being ~2 nm. Also, over CeO_2-R and CeO_2-P materials, clusters containing one or several copper atoms were also observed to densely populate the CeO_2 support. This was not the case with the CeO_2-C based catalyst. The STEM-EDX results are in good agreement with data obtained from the dissociative N_2O adsorption measurements (Table 2).

UV−vis diffuse reflectance spectra of solids containing 2 and 4 wt % of Cu are presented in Figures S2 and S3. All materials containing 2 wt % Cu have two peaks with maxima located at 450−470 nm and 750−800 nm. The first peak could be attributed to Cu^{1+} clusters and/or bis(μ-oxo)dicopper core ($[Cu_2O]^{2+}$), while the second peak is due to d−d Cu^{2+} transition in more or less tetragonally distorted O_h symmetry (these attributions were thoroughly discussed in our previous works[27,28]). Increasing Cu loading to 4 wt % in the case of 4-Cu/CeO_2-C sample results in appearance of an additional absorption peak at 600 nm (Figure S3), which is most likely a consequence of segregated bulk CuO.[28,37,38] Relatively low BET specific surface area of this sample results in poor dispersion of Cu (further confirmed by both N_2O chemisorption experiments and TEM investigation) and formation of larger CuO particles. At the same time, for high surface area CeO_2-R and CeO_2-P based materials, peak at 600 nm appears only for samples with Cu loading higher than 6 wt % (Figure S4).

Additional information on surface Cu oxidation states in Cu/CeO_2 catalysts was obtained by FTIR spectroscopy with adsorbed CO (Figure S5). Position of characteristic Cu-carbonyl peaks is very sensitive to oxidation states of Cu (Cu^{2+}, Cu^{+}, and Cu^{0}). Vibrations belonging to CO adsorbed on Cu sites can be distinguished as (i) Cu^{2+} carbonyl species with absorption above 2140 cm^{-1}, (ii) Cu^{+} carbonyl species with absorption between 2140 and 2110 cm^{-1}, and (iii) Cu^{0}

DOI: 10.1021/acscatal.5b01044
ACS Catal. 2015, 5, 5357−5365

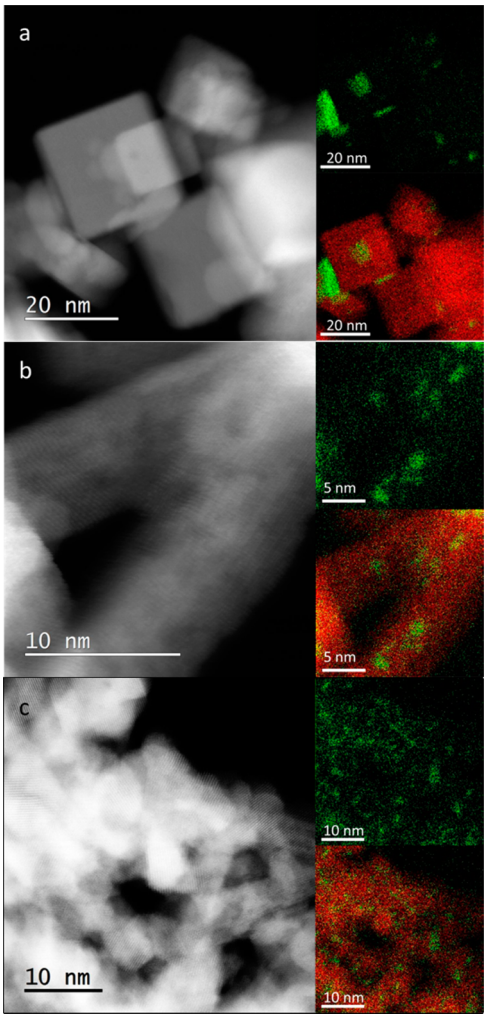

Figure 3. STEM image and EDX mapping of Cu as well as overlay of Ce and Cu distribution observed for 4-Cu/CeO_2-C (a), 4-Cu/CeO_2-R (b), and 4-Cu/CeO_2-P (c) catalysts.

carbonyl species which usually absorb at a frequency lower than 2110 cm^{-1}.[39−44] By applying the second derivative (for resolving the actual number of overlapping peaks, Figures S6−S8) and temperature resolved in situ DRIFT spectroscopy (Figure 4), extraction of valuable information from the apparently simple spectra was possible. For detailed interpretation please refer to the Supporting Information.

Copper carbonyl spectra of CeO_2-C, CeO_2-R, and CeO_2-P based catalysts all exhibit absorption peaks at 2118, 2102, 2092, 2067, and 2056 cm^{-1}; whereas, peaks with maximum at 2140 and 2110 cm^{-1} are characteristic only for 4-Cu/CeO_2-R and 4-Cu/CeO_2-P samples. The presence of Cu^+ defect sites in several-atom Cu clusters, which are visualized over CeO_2-P and CeO_2-R based materials during EDX mapping (Figure 3), results in an additional peak at 2140 cm^{-1} in 4-Cu/CeO_2-R and 4-Cu/CeO_2-P samples that causes broadening of the CO carbonyl signal. Smaller CuO clusters contain more unsaturated and highly reactive surface defect sites, which produce additional absorption bands at higher wavenumbers and broaden the overall CO carbonyl absorption band. The presence of both Cu^0 and Cu^+ sites in Cu/CeO_2 catalysts indicates facile reducibility and occurrence of copper in low oxidation states, which is especially important for utilizing these catalysts in N_2O decomposition reaction.[28]

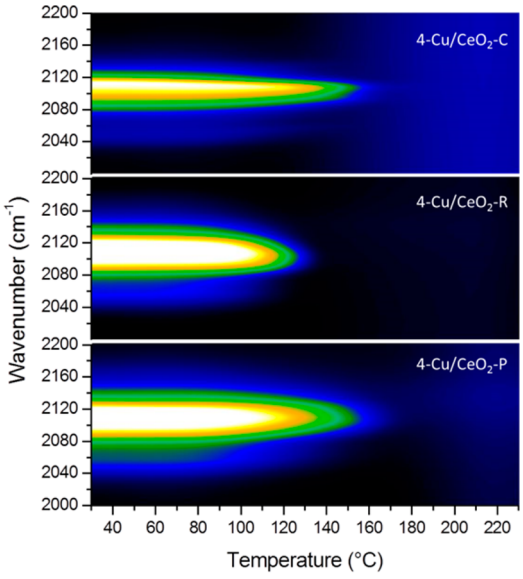

Figure 4. Results of CO-TPD experiments presented as color surfaces for CuO/CeO_2 solids containing 4 wt % of Cu.

Temperature-resolved in situ DRIFTS analysis (Figure 4) revealed different thermal stability of individual Cu-carbonyls in the studied materials. Absorption in the region between 2160 and 2040 cm^{-1} disappeared at 130 °C for 4-Cu/CeO_2-R sample, while Cu carbonyls in 4-Cu/CeO_2-P and 4-Cu/CeO_2-C samples were stable up to 160 °C. Lower stability of carbonyls on the surface of 4-Cu/CeO_2-R solid could be ascribed to easier reduction of Cu^+ sites into Cu^0 by adsorbed CO molecules, indicating superior redox properties of this sample compared to 4-Cu/CeO_2-P and 4-Cu/CeO_2-C materials.

In order to identify surface oxidation state of Cu, X-ray photoelectron spectroscopy was utilized. It is known that Cu electronic state (Cu^0, Cu^+, and Cu^{2+}) can be identified from the position and shape of both photoelectron Cu $2p_{3/2}$ line and Auger Cu L_3VV electron line.[45−47] The lack of shakeup satellites at higher apparent Cu $2p_{3/2}$ binding energy than the main core level indicates the absence of Cu^{2+} species (Figure S9). Furthermore, Cu $2p_{3/2}$ band is centered at 932.3−932.7 eV, which is characteristic of reduced Cu species. The Cu L_3VV Auger line and modified Auger parameter were used to identify Cu electronic state. The Auger kinetic energies for bulk Cu_2O and Cu metal are 916.6 and 918.3 eV, respectively. The Auger Cu L_3VV electron line is centered at about 916.1−917.1 eV, which can be ascribed to the presence of Cu^+. Modified Auger parameter, which was calculated by adding binding energy of Cu $2p_{3/2}$ photoelectron peak and kinetic energy of Cu L_3VV Auger peak, confirms the presence of Cu^+ species on the catalysts surface (Table 3).[46] Therefore, we can conclude that copper in all examined solids exists in Cu^+ oxidation state, which is in line with the results of CO chemisorption experiments.

The Ce 3d core-level XPS spectra for the studied solids basically denote a mixture of both Ce^{4+} and Ce^{3+} oxidation states (Figure 5), indicating that catalyst surface is partially reduced due to oxygen desorption and formation of oxygen vacancies. However, degree of surface CeO_2 reduction significantly alters for different CeO_2 morphologies. XPS spectrum of 4-Cu/CeO_2-P catalyst exhibits six photoelectron peaks corresponding to three pairs of spin−orbit split doublets

DOI: 10.1021/acscatal.5b01044
ACS Catal. 2015, 5, 5357−5365

Table 3. Results of XPS Analysis

sample	Cu $2p_{3/2}$ BE (eV)	Cu L_3VV KE (eV)	Cu Auger parameter α' (eV)	Ce^{3+} content (%)
4-Cu/CeO_2-C	932.7	917.1	1849.8	33
4-Cu/CeO_2-R	932.6	916.1	1848.7	41
4-Cu/CeO_2-P	932.3	916.7	1849.0	26

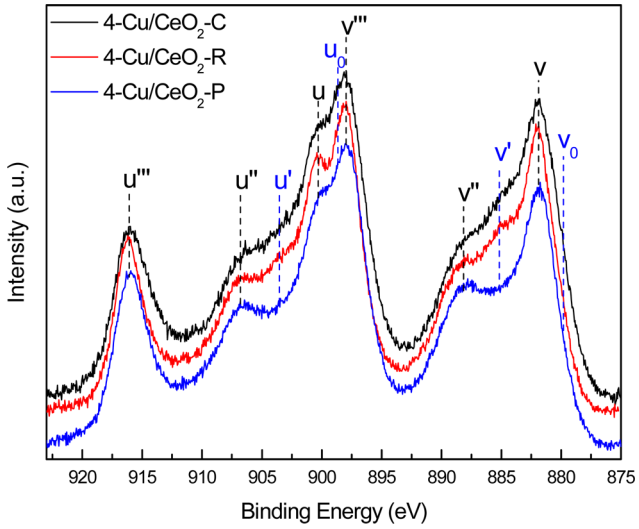

Figure 5. Ce 3d XPS spectra of catalysts containing 4 wt % of Cu.

(v, v″, v‴, u, u″, and u‴), which can be ascribed to 4f configuration of Ce^{4+} ion.[48−52] The appearance of new photoelectron peaks at 885.1 and 903.6 eV (v′ and u′) as well as peak broadening at 879.8 and 898.7 eV (v_0 and u_0) for 4-Cu/CeO_2-C and 4-Cu/CeO_2-R samples provides an evidence of the presence of Ce^{3+}.[51−53] The percentages of Ce^{4+} and Ce^{3+} in the studied solids were determined after Spline linear baseline subtraction and by fitting of Ce 3d core-level XPS spectra with symmetric Gaussian−Lorentzian functions. Results of deconvolution are presented in Figures S10−S12 and Table 3. Observed difference regarding the amount of ceria present in Ce^{3+} oxidation state (33% for 4-Cu/CeO_2-C, 41% for 4-Cu/CeO_2-R and 26% for 4-Cu/CeO_2-P) originates from the exposed surface planes of nanoshaped CeO_2 supports. CeO_2-C and CeO_2-R samples expose {100} and {110} surface planes; desorption of oxygen from these surfaces occurs more easily, which results in higher Ce^{3+} content. On the other hand, CeO_2-P material predominantly exposes the most stable {111} planes; therefore, the extent of Ce^{3+} in 4-Cu/CeO_2-P sample is lower. These results are in good agreement with the work of Sreeremya et al., where the highest concentration of Ce^{3+} (44.3%) was found in the sample containing ceria nanorods and nanocubes, while in polyhedral CeO_2 only 26.2% of Ce^{3+} was present.[54]

The lability of oxygen in the structure of Cu/CeO_2-R catalysts was evaluated using H_2-TPR analysis (Figure S13). Reduction of studied catalysts occurred between 50 and 150 °C. Co-reduction of the CeO_2 support is confirmed by quantifying H_2 consumption, which greatly surpasses the theoretical values, required for complete reduction of CuO to Cu^0 (Table S1). H_2 consumed for CeO_2 reduction is very similar for all CeO_2-R based materials, regardless of Cu loading and equals to 13.2 ± 1 cm^3/g. This value is comparable to H_2 consumed for surface reduction of bare CeO_2-R, 10.4 cm^3/g (Figure 1 and Table 1). Reduction of Cu/CeO_2-R materials occurring at temperatures significantly lower than those of individual CuO and CeO_2 components is due to electronic interactions between the two oxide phases that weaken the metal−oxygen bonds (so-called "synergetic effect").[55,56] For samples with higher Cu loading, reduction peaks shift to higher temperatures, which is due to lower Cu dispersion and increase of CuO cluster size (confirmed by N_2O titration experiments).

Figure 6 and Table S1 provide H_2-TPR results for samples containing 4 wt % of Cu supported on differently nanoshaped

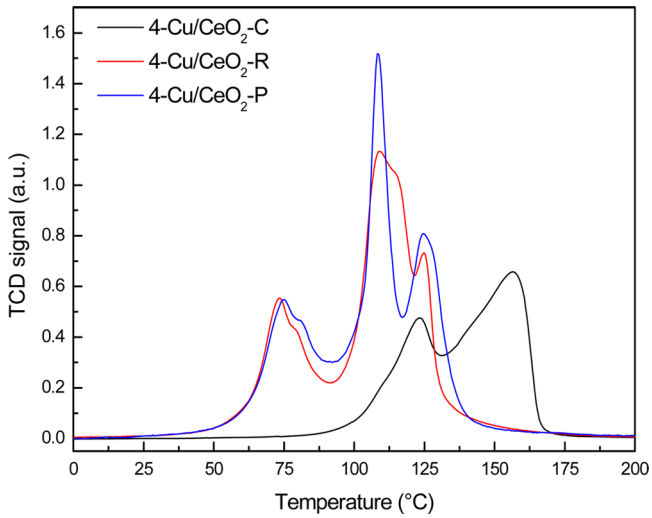

Figure 6. H_2-TPR profiles of CuO/CeO_2 catalysts containing 4 wt % of Cu.

CeO_2 supports (i.e., CeO_2-C, CeO_2-R, and CeO_2-P). The amount of H_2 consumed for reduction of CeO_2 support correlates with BET specific surface area of analyzed materials (CeO_2-P > CeO_2-R > CeO_2-C) and is very similar to the values obtained during reduction of pure CeO_2. Reduction profiles significantly differ among examined solids and depend on morphology of CeO_2 support. Reduction of 4-Cu/CeO_2-C sample occurs at temperatures 50 °C higher than for CeO_2-R and CeO_2-P based catalysts. This phenomenon is caused by lower CuO dispersion and formation of larger CuO particles as well as bulk CuO aggregates (up to 15 nm) on CeO_2-C support.

3.2. Catalytic N_2O Decomposition. N_2O conversions obtained over nanoshaped Cu/CeO_2 catalysts as a function of reaction temperature exhibit typical S-shaped curves (Figures S14−S16). Synthesized materials show excellent catalytic stability, which was confirmed by long-term stability tests in the period of 50 h time on stream (Figure S17). Activation energies (Table 4) vary from 87 to 102 kJ/mol for solids containing 4 wt % of Cu. Table S2 shows a comparison of E_a calculated in this work and activation energies for materials (Cu/ZSM-5, Cu/Al_2O_3, Co/ZSM-5, Fe/ZSM-5) utilized for N_2O decomposition by other research groups.[57−59] The activation energy for 4-Cu/CeO_2-R sample is about 43−64 kJ/mol lower than E_a values for other Cu based solids.

Activity, expressed per amount of copper (Figure 7) goes through a maximum at 4 wt % Cu loading for all nanoshaped CeO_2 supports. Catalysts based on CeO_2-C support demonstrate lower activity over the whole concentration range of

DOI: 10.1021/acscatal.5b01044
ACS Catal. 2015, 5, 5357−5365

Table 4. Catalytic Properties of Nanoshaped CeO_2 Supported CuO Catalysts

sample	E_a (kJ/mol)	activity[a]	A_{norm}[b] (min^{-1})
4-Cu/CeO_2-C	102	28.2	0.130
4-Cu/CeO_2-R	87	63.2	0.138
4-Cu/CeO_2-P	92	58.0	0.111

[a]Activity measured in μmol(N_2O)/(mmol(Cu) min) at T = 375 °C. [b]Normalized activity measured at T = 375 °C by counting surface Cu atoms determined by means of dissociative N_2O chemisorption.

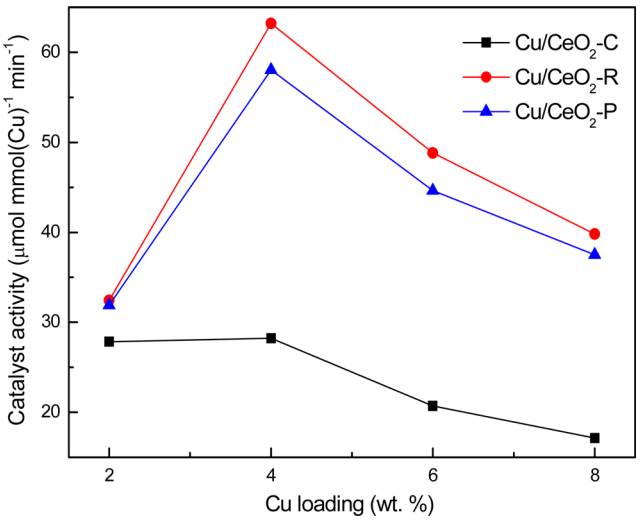

Figure 7. Activity of nanoshaped CuO/CeO_2 catalysts measured at T = 375 °C.

deposited Cu, compared to CeO_2-P and especially CeO_2-R based solids. Small CuO clusters possess the highest activity in N_2O decomposition reaction, while either atomically dispersed copper or bulk CuO phase have lower intrinsic catalytic activity.[28] This is due to the requirement of at least two adjacent Cu atoms to favor merging of two oxygen atoms and its desorption as molecular oxygen.[27] According to a tentative mechanism of nitrous oxide decomposition that we propose, N_2O molecule adsorbs on Cu^+ active sites and, after N−O bond cleavage accompanied by N_2 molecule liberation, formation of Cu^{2+}−O^- species takes place (eqs 1 and 2). Regeneration of active Cu^+ sites can be achieved either by a recombination step (if two oxidized copper sites are close enough to each other) or through reduction by Ce^{3+} (eqs 3 and 4). The latter step is likely to occur because of synergetic effect and high lattice oxygen mobility between CuO and CeO_2 active phases, which is confirmed by results of H_2-TPR examination. Formed Ce^{4+} can further desorb oxygen and regenerate oxygen vacancy and Ce^{3+} species (eq 5).

$$Cu^+ + ONN \rightarrow Cu^+{-}ONN \quad (1)$$

$$Cu^+{-}ONN \rightarrow Cu^{+2}{-}O^- + N_2 \quad (2)$$

$$2Cu^{+2}{-}O^- \rightarrow 2Cu^+ + O_2 \quad (3)$$

$$Cu^{+2}{-}O^- + Ce^{+3} \rightarrow Cu^+ + Ce^{+4}{-}O^- \quad (4)$$

$$2Ce^{+4}{-}O^- \rightarrow 2Ce^{+3} + O_2 \quad (5)$$

Lower intrinsic activity of copper sites in bulk CuO clusters originates from their lower surface energy as a result of higher coordination and lower number of very active defect sites. Therefore, no improvement in catalytic activity for materials containing more than 4 wt % Cu could be attributed to lower Cu dispersion as well as formation of larger CuO clusters, which was confirmed by results of DR UV−vis and H_2-TPR experiments.

By comparing the activity of catalysts, normalized per number of surface Cu atoms (A_{norm} = $n(N_2O)_{decomposed}$/[$n(Cu)_{surf}$ × time]) (Figure 8 and Table 4), shape-dependent

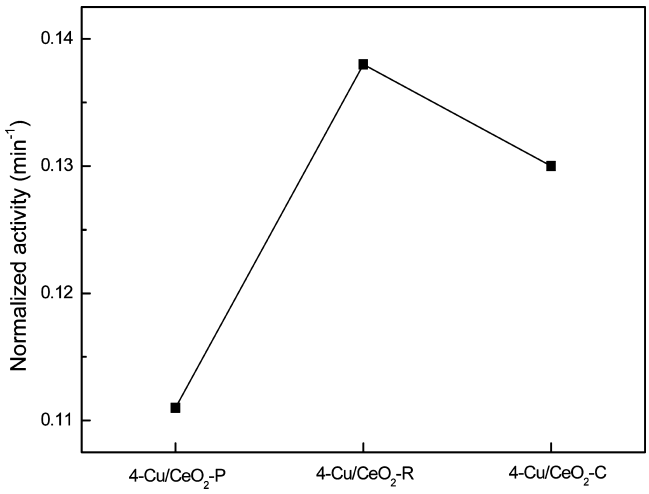

Figure 8. Normalized activity for nanoshaped CuO/CeO_2 catalysts measured at T = 375 °C.

activity of CuO/CeO_2 catalysts is revealed, indicating higher activity of copper deposited over the {100} and {110} planes of CeO_2 support. The A_{norm} value for 4-Cu/CeO_2-P sample is around 20% lower in comparison with corresponding CeO_2 nanocubes and nanorods based samples (0.130 min^{-1} for 4-Cu/CeO_2-C, 0.138 min^{-1} for 4-Cu/CeO_2-R, and 0.111 min^{-1} for 4-Cu/CeO_2-P).

Above-mentioned results signify the effect of exposed surface planes of ceria support on the catalyst reactivity in N_2O decomposition. We can claim that copper clusters supported on {100} and {110} surface planes of CeO_2 are more active compared to clusters deposited on {111} planes of CeO_2-P support. It was shown by theoretical investigation that {100} and {110} surface planes possess lower activation energy for oxygen desorption and formation of anion vacancies than {111} surface plane of CeO_2 (2.26, 2.1, and 2.76 eV, respectively), which allows easier oxygen desorption and formation of oxygen vacancies.[22] We have confirmed this fact by results of XPS examination, where formation of Ce^{3+} was favored on ceria nanorods and nanocubes based samples, while polyhedral ceria surface with {111} planes contains less Ce^{3+} ions. Strong interaction between CeO_2 support and active Cu phase (confirmed by H_2-TPR examination) further promotes oxygen mobility between two phases and enables easier oxygen desorption especially in the case where Cu clusters populate {100} and {110} surface planes. The above-mentioned steps are crucial in the N_2O decomposition mechanism, which implies that A_{norm} values of CuO/CeO_2 catalysts are highly sensitive to surface planes exposed by the ceria support. To sum up, combination of very reactive {100} and {110} surface planes of ceria nanorods support with high values of BET specific surface area and Cu dispersion results in superior catalytic properties of CeO_2-R based solids.

DOI: 10.1021/acscatal.5b01044
ACS Catal. 2015, 5, 5357−5365

4. CONCLUSIONS

The lability of surface oxygen atoms in nanoshaped CeO_2 depends on the exposed crystalline planes and defect sites and decreases in the following order: CeO_2-R > CeO_2-C > CeO_2-P. Accordingly to DRIFTS examination, surface Cu is present as Cu^+ and Cu^0 oxidation states. XPS analysis shows that under high vacuum, surface of CeO_2-R and CeO_2-C solids is enriched with Ce^{3+} (41 and 33%, correspondingly), while the one in CeO_2-P sample has the lowest Ce^{3+} content (26%).

Deposition of copper decreases the initiation of CeO_2 reduction by about 150 °C, but the extent of its reduction is only negligibly influenced by copper addition. Cu clusters populating easily reducible {100} and {110} planes of CeO_2, as preferentially exposed on CeO_2-R and CeO_2-C supports, exhibit normalized activity about 20% higher, compared to copper on {111} planes of CeO_2-P. The most likely reasons for the observed catalytic performance are mainly produced from combination of more reactive {110} and {100} planes exposed on the CeO_2 nanorod surface with high BET specific surface area of this support, the latter enabling higher active metal dispersion and formation of highly reducible copper defect sites.

■ ASSOCIATED CONTENT

Supporting Information

The Supporting Information is available free of charge on the ACS Publications website at DOI: 10.1021/acscatal.5b01044.

Interpretation of DRIFTS results, Tables S1 and S2, and Figures S1–S17 (PDF)

■ AUTHOR INFORMATION

Corresponding Author

*E-mail: albin.pintar@ki.si.

Notes

The authors declare no competing financial interest.

■ ACKNOWLEDGMENTS

The authors gratefully acknowledge the financial support of the Ministry of Education, Science and Sport of the Republic of Slovenia through Research program P2-0150. O.P.T. and L.M.K. specially thank the Russian Science Foundation (Grant No. 14-50-00126) for support.

■ REFERENCES

(1) Delgado, J. J.; del Rio, E.; Chen, X.; Blanco, G.; Pintado, J. M.; Bernal, S.; Calvino, J. J. In *Catalysis by Ceria and Related Materials, Catalytic Science Series*; Trovarelli, A., Fornasiero, P., Eds.; Imperial College Press: London, 2013; Vol. *12*, pp 47–138.

(2) Adijanto, L.; Sampath, A.; Yu, A. S.; Cargnello, M.; Fornasiero, P.; Gorte, R. J.; Vohs, J. M. *ACS Catal.* **2013**, *3*, 1801–1809.

(3) Corma, A.; Atienzar, P.; García, H.; Chane-Ching, J.-Y. *Nat. Mater.* **2004**, *3*, 394–397.

(4) Deng, W.; Flytzani-Stephanopoulos, M. *Angew. Chem., Int. Ed.* **2006**, *45*, 2285–2289.

(5) Cargnello, M.; Gentilini, C.; Montini, T.; Fonda, E.; Mehraeen, S.; Chi, M.; Herrera-Collado, M.; Browning, N. D.; Polizzi, S.; Pasquato, L.; Fornasiero, P. *Chem. Mater.* **2010**, *22*, 4335–4345.

(6) Edwards, J. K.; Pritchard, J.; Lu, L.; Piccinini, M.; Shaw, G.; Carley, A. F.; Morgan, D. J.; Kiely, C. J.; Hutchings, G. J. *Angew. Chem., Int. Ed.* **2014**, *53*, 2381–2384.

(7) Cargnello, M.; Delgado Jaén, J. J.; Hernández Garrido, J. C.; Bakhmutsky, K.; Montini, T.; Calvino Gámez, J. J.; Gorte, R. J.; Fornasiero, P. *Science* **2012**, *337*, 713–717.

(8) Liu, L.; Yao, Z.; Deng, Y.; Gao, F.; Liu, B.; Dong, L. *ChemCatChem* **2011**, *3*, 978–989.

(9) Li, Y.; Wei, Z.; Gao, F.; Kovarik, L.; Peden, C. H. F.; Wang, Y. *J. Catal.* **2014**, *315*, 15–24.

(10) Si, R.; Flytzani-Stephanopoulos, M. *Angew. Chem., Int. Ed.* **2008**, *47*, 2884–2887.

(11) Aneggi, E.; Wiater, D.; de Leitenburg, C.; Llorca, J.; Trovarelli, A. *ACS Catal.* **2014**, *4*, 172–181.

(12) Jiang, Y.; Adams, J. B.; van Schilfgaarde, M. *J. Chem. Phys.* **2005**, *123*, 64701.

(13) Sayle, D. C.; Maicaneanu, S. A.; Watson, G. W. *J. Am. Chem. Soc.* **2002**, *124*, 11429–11439.

(14) Skorodumova, N. V.; Baudin, M.; Hermansson, K. *Phys. Rev. B: Condens. Matter Mater. Phys.* **2004**, *69*, 075401.

(15) Vilé, G.; Colussi, S.; Krumeich, F.; Trovarelli, A.; Pérez-Ramírez, J. *Angew. Chem., Int. Ed.* **2014**, *53*, 12069–12072.

(16) Zhou, G.; Gui, B.; Xie, H.; Yang, F.; Chen, Y.; Chen, S.; Zheng, X. *J. Ind. Eng. Chem.* **2014**, *20*, 160–165.

(17) Huang, H.; Dai, Q.; Wang, X. *Appl. Catal., B* **2014**, *158–159*, 96–105.

(18) Désaunay, T.; Bonura, G.; Chiodo, V.; Freni, S.; Couzinié, J.-P.; Bourgon, J.; Ringuedé, A.; Labat, F.; Adamo, C.; Cassir, M. *J. Catal.* **2013**, *297*, 193–201.

(19) Monte, M.; Gamarra, D.; López Cámara, A.; Rasmussen, S. B.; Gyorffy, N.; Schay, Z.; Martínez-Arias, A.; Conesa, J. C. *Catal. Today* **2014**, *229*, 104–113.

(20) Mann, A. K. P.; Wu, Z.; Calaza, F. C.; Overbury, S. H. *ACS Catal.* **2014**, *4*, 2437–2448.

(21) Ta, N.; Liu, J.; Shen, W. *Chin. J. Catal.* **2013**, *34*, 838–850.

(22) Mayernick, A. D.; Janik, M. J. *J. Phys. Chem. C* **2008**, *112*, 14955–14964.

(23) Santiago, M.; Pérez-Ramírez, J. *Environ. Sci. Technol.* **2007**, *41*, 1704–1709.

(24) Pérez-Ramírez, J.; Kapteijn, F.; Schöffel, K.; Moulijn, J. A. *Appl. Catal., B* **2003**, *44*, 117–151.

(25) Adamski, A.; Zając, W.; Zasada, F.; Sojka, Z. *Catal. Today* **2012**, *191*, 129–133.

(26) Zhou, H.; Huang, Z.; Sun, C.; Qin, F.; Xiong, D.; Shen, W.; Xu, H. *Appl. Catal., B* **2012**, *125*, 492–498.

(27) Zabilskiy, M.; Erjavec, B.; Djinović, P.; Pintar, A. *Chem. Eng. J.* **2014**, *254*, 153–162.

(28) Zabilskiy, M.; Djinović, P.; Erjavec, B.; Dražić, G.; Pintar, A. *Appl. Catal., B* **2015**, *163*, 113–122.

(29) Wuebbles, D. J. *Science* **2009**, *326*, 56–57.

(30) Ravishankara, A. R.; Daniel, J. S.; Portmann, R. W. *Science* **2009**, *326*, 123–125.

(31) Ramaswamy, A. V. In *Catalysis: principles and applications*; Viswanathan, B., Sivasanker, S., Ramaswamy, A. V., Eds.; Narosa publishing house: New Delhi, 2002; pp 206–219.

(32) Fichtl, M. B.; Schumann, J.; Kasatkin, I.; Jacobsen, N.; Behrens, M.; Schlögl, R.; Muhler, M.; Hinrichsen, O. *Angew. Chem., Int. Ed.* **2014**, *53*, 7043–7047.

(33) Osojnik Črnivec, I. G.; Djinović, P.; Erjavec, B.; Pintar, A. *Chem. Eng. J.* **2012**, *207–208*, 299–307.

(34) Yao, H. C.; Yao, Y. F. Y. *J. Catal.* **1984**, *86*, 254–265.

(35) Giordano, F.; Trovarelli, A.; de Leitenburg, C.; Giona, M. *J. Catal.* **2000**, *193*, 273–282.

(36) Hosokawa, S.; Imamura, S.; Iwamoto, S.; Inoue, M. *J. Eur. Ceram. Soc.* **2011**, *31*, 2463–2470.

(37) Zhu, Z. H.; Zhu, H. Y.; Wang, S. B.; Lu, G. Q. *Catal. Lett.* **2003**, *91*, 73–81.

(38) Marion, M. C.; Garbowski, E.; Primet, M. *J. Chem. Soc., Faraday Trans.* **1990**, *86*, 3027–3032.

(39) Dandekar, A.; Vannice, M. A. *J. Catal.* **1998**, *178*, 621–639.

(40) Hanson, J. C.; Si, R.; Xu, W.; Senanayake, S. D.; Mudiyanselage, K.; Stacchiola, D.; Rodriguez, J. A.; Zhao, H.; Beyer, K. A.; Jennings, G.; Chapman, K. W.; Chupas, P. J.; Martínez-Arias, A. *Catal. Today* **2014**, *229*, 64–71.

DOI: 10.1021/acscatal.5b01044
ACS Catal. 2015, 5, 5357–5365

(41) Kydd, R.; Ferri, D.; Hug, P.; Scott, J.; Teoh, W. Y.; Amal, R. *J. Catal.* **2011**, *277*, 64−71.
(42) Sato, A. G.; Volanti, D. P.; Meira, D. M.; Damyanova, S.; Longo, E.; Bueno, J. M. C. *J. Catal.* **2013**, *307*, 1−17.
(43) Padley, M. B.; Rochester, C. H.; Hutchings, G. J.; King, F. *J. Catal.* **1994**, *148*, 438−452.
(44) Hollins, P. *Surf. Sci. Rep.* **1992**, *16*, 51−94.
(45) Shpiro, E. S.; Grunert, W.; Joyner, R. W.; Baeva, G. N. *Catal. Lett.* **1994**, *24*, 159−169.
(46) Biesinger, M. C.; Lau, L. W. M.; Gerson, A. R.; Smart, R. S. C. *Appl. Surf. Sci.* **2010**, *257*, 887−898.
(47) Colussi, S.; Amoroso, F.; Katta, L.; Llorca, J.; Trovarelli, A. *Catal. Lett.* **2014**, *144*, 1023−1030.
(48) Skála, T.; Šutara, F.; Prince, K. C.; Matolín, V. *J. Electron Spectrosc. Relat. Phenom.* **2009**, *169*, 20−25.
(49) Yang, F.; Graciani, J.; Evans, J.; Liu, P.; Hrbek, J.; Sanz, J. F.; Rodriguez, J. A. *J. Am. Chem. Soc.* **2011**, *133*, 3444−3451.
(50) Reddy, B. M.; Khan, A.; Yamada, Y.; Kobayashi, T.; Loridant, S.; Volta, J.-C. *J. Phys. Chem. B* **2003**, *107*, 5162−5167.
(51) Pfau, A.; Schierbaum, K. D. *Surf. Sci.* **1994**, *321*, 71−80.
(52) Rodriguez, J. A.; Ma, S.; Liu, P.; Hrbek, J.; Evans, J.; Pérez, M. *Science* **2007**, *318*, 1757−1760.
(53) Kugai, J.; Subramani, V.; Song, C.; Engelhard, M. H.; Chin, Y.-H. *J. Catal.* **2006**, *238*, 430−440.
(54) Sreeremya, T. S.; Krishnan, A.; Remani, K. C.; Patil, K. R.; Brougham, D. F.; Ghosh, S. *ACS Appl. Mater. Interfaces* **2015**, *7*, 8545−8555.
(55) Zhou, K.; Xu, R.; Sun, X.; Chen, H.; Tian, Q.; Shen, D.; Li, Y. *Catal. Lett.* **2005**, *101*, 169−173.
(56) Chen, J.; Zhan, Y.; Zhu, J.; Chen, C.; Lin, X.; Zheng, Q. *Appl. Catal., A* **2010**, *377*, 121−127.
(57) Smeets, P. J.; Sels, B. F.; van Teeffelen, R. M.; Leeman, H.; Hensen, E. J. M.; Schoonheydt, R. A. *J. Catal.* **2008**, *256*, 183−191.
(58) Dandekar, A.; Vannice, M. A. *Appl. Catal., B* **1999**, *22*, 179−200.
(59) Kapteijn, F.; Marban, G.; Rodriguez-Mirasol, J.; Moulijn, J. A. *J. Catal.* **1997**, *167*, 256−265.

DOI: 10.1021/acscatal.5b01044
ACS Catal. 2015, 5, 5357−5365